Supplementary Material for

Scalable plasmonic physical unclonable functions empowered by a multi-dimensional expanding strategy

Juntao Duan,[a,†] Guoqun Li,[b,†] Yizhe Xiong,[a] Xiangnan Zhu,[b] Yan Chen,[d] Wei Liu,[a,c] Xiaochuan Xu,[a,c] Perry Ping Shum,[e,*] Qi Hao,[b,*] Jiawei Wang[a,c,*]

[a]Harbin Institute of Technology (Shenzhen), School of Integrated Circuits, Shenzhen, China, 518055

[b]Southeast University, Key Laboratory of Quantum Materials and Devices of Ministry of Education, School of Physics, Nanjing, China, 211189

[c]Harbin Institute of Technology, National Key Laboratory of Laser Spatial Information, Shenzhen, China, 518055

[d]National University of Defense Technology, College of Advanced Interdisciplinary Studies, Changsha, China, 410073

[e]Southern University of Science and Technology, Department of Electronic and Electrical Engineering, Shenzhen, China, 518055

[†] These authors contributed equally to this work.

[*] Address all correspondence to Jiawei Wang, Qi Hao, Perry Ping Shum

Email: wangjw7@hit.edu.cn; qihao@seu.edu.cn; shenp@sustech.edu.cn

The PDF file includes:

Section S1. Details in the nanomembrane template-assisted fabrication

The fabrication of anodic aluminum oxide (AAO) membranes followed a previously reported anodization procedure.[45, 46] Initially, the AAO membranes with small pores on aluminum foils underwent etching in a 5% phosphoric acid solution at 30 ℃ for 27 minutes to expand the initial pores. Subsequently, a thin protective layer of Poly (methyl methacrylate) (PMMA) was applied to the pores using a spin-coating method. The coated membranes were baked at 120 ℃ for 15 minutes to ensure complete pore filling. Following this, the membranes were immersed in a 5% NaOH solution for 15 minutes, then promptly transferred to a $CuCl_2$ solution to fully remove the aluminum substrate. The remaining membranes underwent an additional treatment in a phosphoric acid (5%) - $CuCl_2$ (2%) mixed solution for 35 minutes to remove the barrier layer and tune the pore thickness. The membranes were subsequently placed in acetone to remove the PMMA protective layer. Finally, the freestanding AAO membranes were thoroughly cleaned with distilled water and transferred onto substrates for electron-beam evaporation. The resulting membranes possess a pore diameter of ~ 80 nm and a thickness of ~ 276 nm after the etching process.

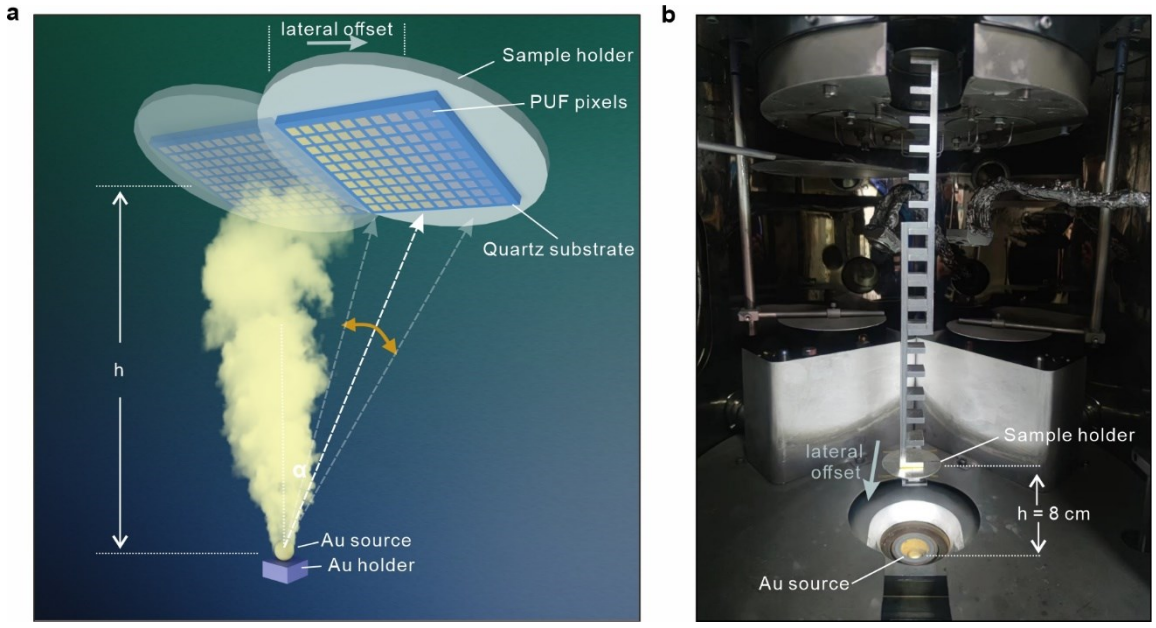

Fig. S1 (a) Schematic showing the fabrication of heterogeneous nanoparticle arrays by angle-resolved shadow deposition. (b) Picture of the deposition system, with the adjusted vertical height *h* and lateral offset denoted.

The substrates integrated with AAO membranes were placed on a plane stage. As illustrated in

Fig. S1(a), angle-resolved shadow evaporation was realized by shifting the location of the stage loaded with substrates. Compared with our previous studies employing shadow deposition,[47] the vertical height *h* between the sample and the source is significantly reduced (see Fig. S1(a)-(b)), while there is no tilting of the substrates. Besides, the deposition angle α gets changed accordingly by changing the offset distance *d* away from the central point ($\alpha = 0°$). Due to the existence of α, the evaporation paths might be partly blocked by the AAO pores. Upon a large deposition angle, some atoms are blocked by the pore walls of the nanomembrane template. This results in a reduced amount of the atoms being deposited onto the substrate, and hence an overall gradience of particle size as presented in Fig. 2(f)-(g) in the main article.

By setting *h* of ~ 8 cm and *d* of ~ 1.5 cm, our calculation result suggests that a variation of α between 8° and 16° can be obtained on a single centimeter-sized chip. The evaporation path is completely blocked when the value α extends this range. One should note that the clusters of nanoparticles are formed due to random defects and impurities. For samples made with $\alpha = 8°$, 20 clusters were inspected via scanning electron microscopy (SEM), suggesting an average size of ~ 5.3 μm.

Section S2. Properties of deposited nanostructure upon different angles

For deposited plasmonic structures fabricated at varying α between 8° and 16°, the scales of clusters and nanoparticles vary significantly. For the characterized SEM images, one can analyze the statistics of the nanoparticle sizes using ImageJ software. The distribution of gold nanoparticles with α = 8° and α = 16° within an area of ~ 2 μm² was quantified (see Fig. S2). The averaged particle size at α = 16° is ~ 50% smaller than that at α = 8°.

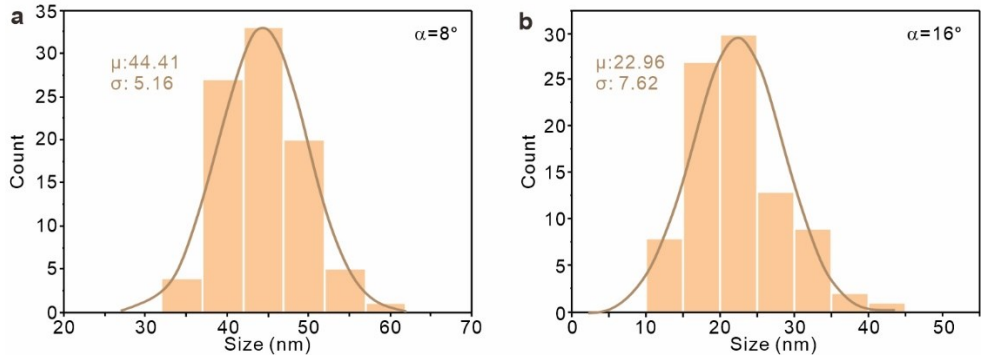

Fig. S2 The histograms of nanoparticle size with α = 8° (a) and 16° (b).

Alternatively, the optical responses can be revealed by dark-field imaging. Here we performed the characterization using an inverted microscope system (ECLIPSE Ti2-U, Nikon). The scattering images were captured using an objective (TU Plan Fluor 50×, NA=0.8) and CCD (DS-Ri2, Nikon). As revealed in Fig. S3, the bright spots are attributed to the clusters of nanoparticles. Overall, compared with the sample made at α = 16°, one can discern much stronger scattering signals with spatial inhomogeneity for the same of α = 8°.

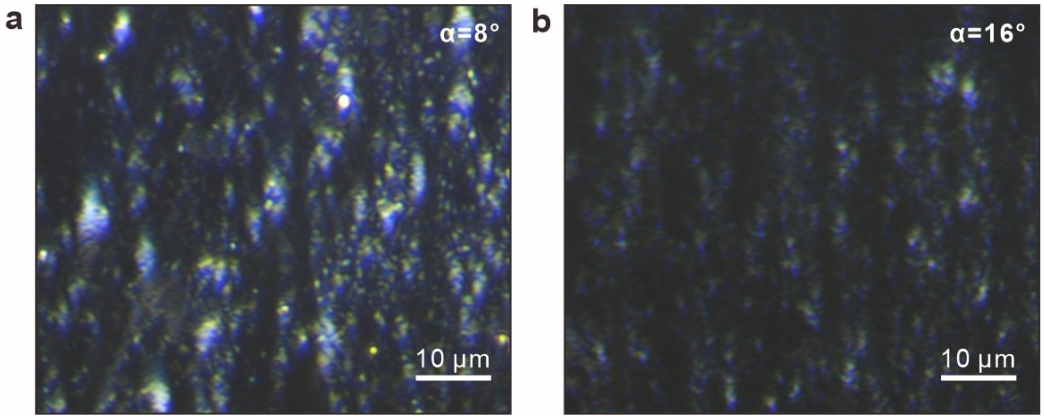

Fig. S3 Dark field microscopy images for PUF labels with α = 8° (a) and 16° (b).

Based on our home-built hyperspectral imaging setup, one can study the extinction spectra of samples with varying α. As depicted in Fig. S4, the overall blueshift of LSPRs for a larger α is consistent. Meanwhile, the extinction is weakened upon a larger α (more statistics are shown in Fig. S5). As an example, the lower extinction at α = 16° can be discernable from the overall profile of the transmission image in Fig. S6(a) and also the distribution of the pixel values (see Fig. S6(b)).

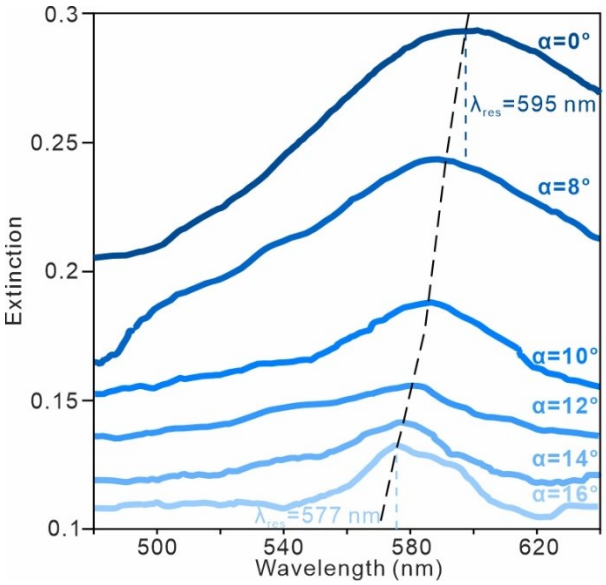

Fig. S4 Extinction spectra for PUF labels with varying deposition angles. The black dashed line serves as a visual aid.

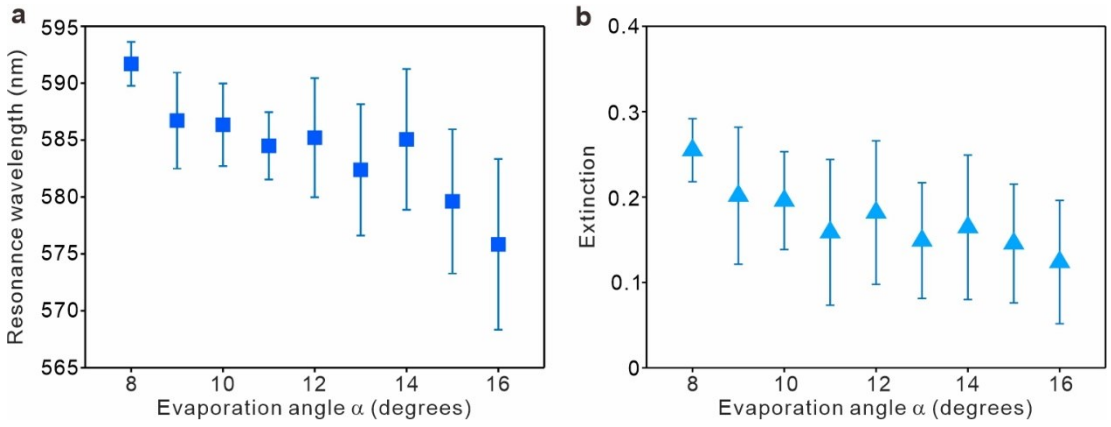

Fig. S5 Summarized properties of LSPRs of plasmonic samples with different PUF labels fabricated on the same substrate. (a) Resonance wavelength as a function of α. (b) Extinction spectra peak value as a function of α.

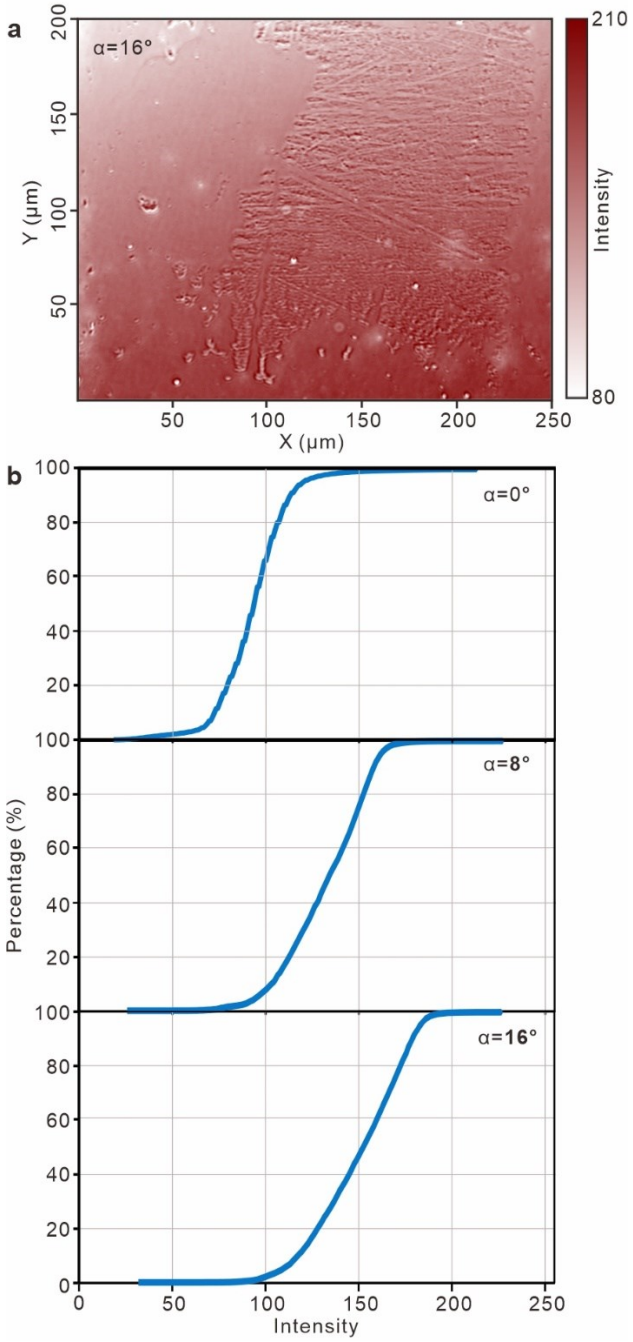

Fig. S6 (a) Captured transmission image for the PUF with α = 16°. (b) The cumulative curve of the digitized intensity for three PUF labels with α = 0° (top), 8° (middle), and 16° (bottom).

Upon a large deposition angle, some atoms are blocked by the pore walls of the nanomembrane template, resulting in a reduced amount of the atoms being deposited onto the substrate, and hence an overall gradience of particle size. Figure S7 shows the SEM images when the deposition angles are respectively 9°, 11°, 13° and 15°.

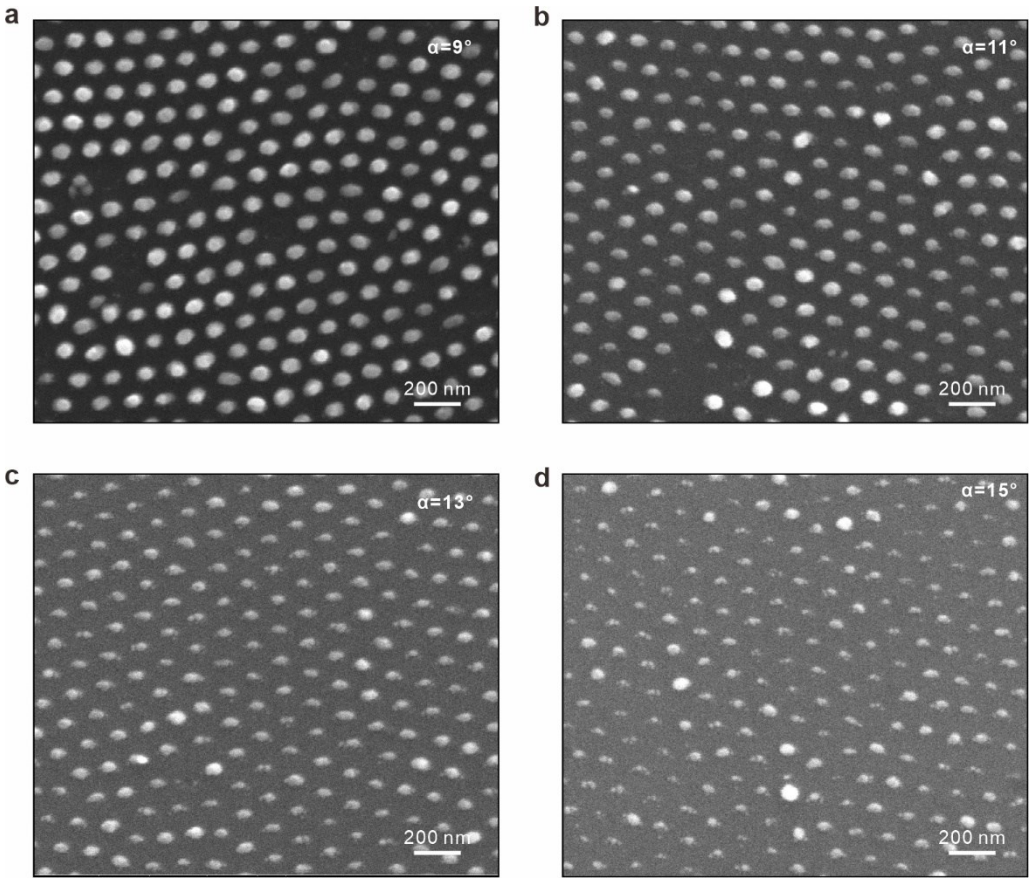

Fig. S7 SEM images of PUF labels fabricated with α = 9° (a), 11° (b), 13° (c) and 15° (d).

Section S3. Details of examining the uniqueness and reproducibility

For quantifying the uniqueness using inter-device HD, 15 PUF labels with the same *N* and different *M* (1-15) were characterized. Figure S8(a) summarizes the raw transmission images, and Fig. S8(b) presents the corresponding PUF keys with a size of 30 × 30.

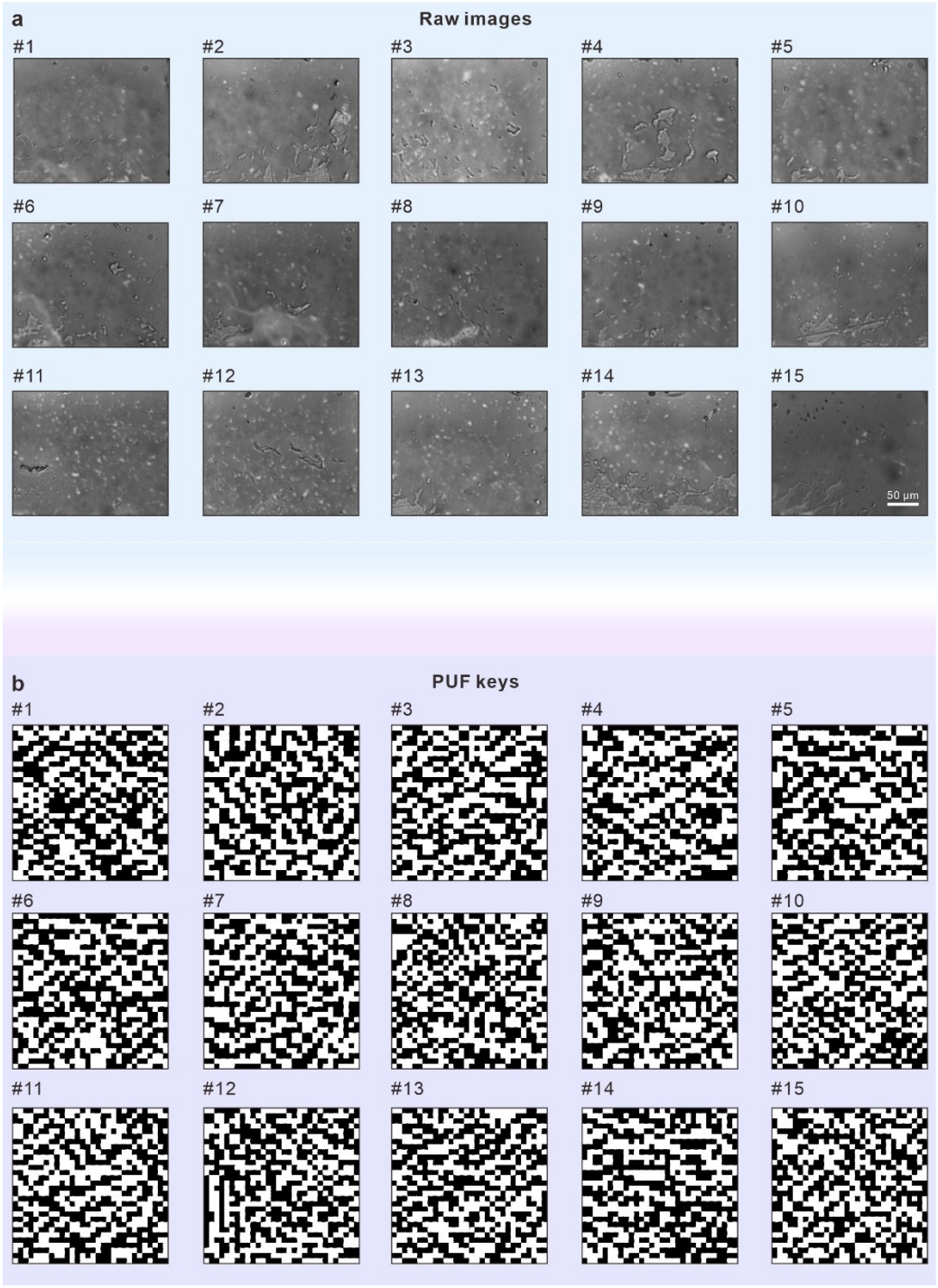

Fig. S8 (a) Raw images obtained from 15 PUF labels with the same N. (b) The corresponding 15 PUF keys with a size of 30 × 30.

Figure S9 summarizes the intra-device HD based on 15 repeated challenge-response cycles for the same PUF (α = 8° as an example) in one hour. The 2D correlation map suggests the intra-device HD values are all below 0.0122, which is far apart from the preset threshold of 0.03.

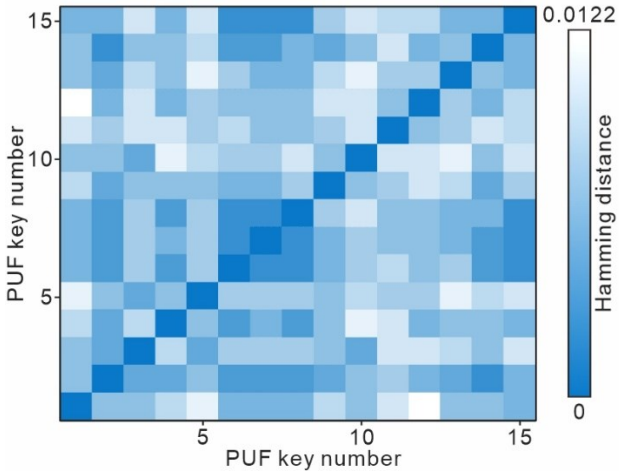

Fig. S9 Pairwise match of 15 PUF keys repeatedly measured from the same PUF label (α= 8°) to examine the reproducibility.

Section S4. PUF stability tests in real-world scenarios

Firstly, the stability of plasmonic PUFs against humidity variations was tested. Industrial hygrometers (CX-601, YIDU) were used to measure relative humidity (RH). RH of the local environment was adjusted using a humidifier. The variation in HD was tracked for varying RH levels between 39% to 68% (see Fig. S10(a)). One can discern that the HD is always lower than the preset threshold of 0.03, indicating nice reproducibility.

Secondly, the long-term test was carried out for a single PUF for eight consecutive days (twice per day, at 14:00 and 19:00). Again, the extracted HD is always lower than the preset threshold of 0.03 (see Fig. S10(b)).

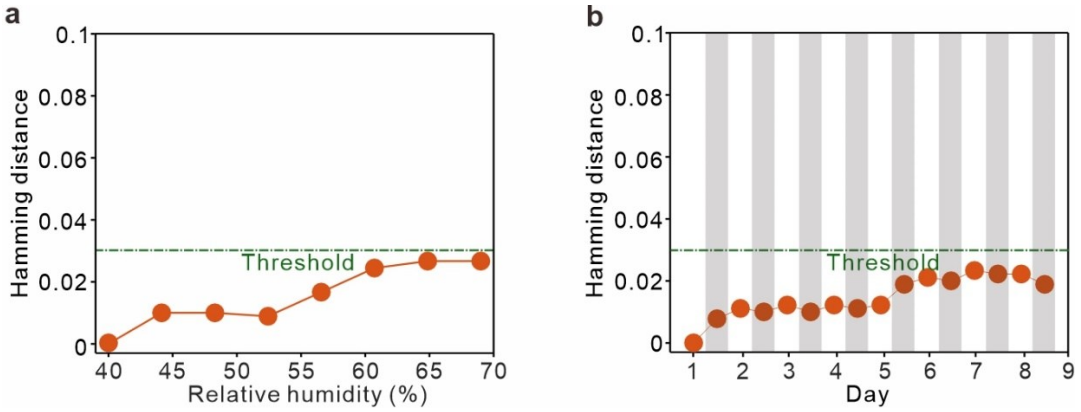

Fig. S10 Tracked HD of one single PUF. (a) Over a change in relative humidity between 39% and 68%. (b) Measured at noon (white area) and evening (gray area) over 8 days.

Section S5. Performance of PUFs upon an expanded capacity

In the main article, the 900-bit PUF keys yield a characterized capacity of ~ 2^{875} based on the estimated mutually independent bits. Given the nature of pHash algorithm, the PUF keys are scalable. Figure S11 summarizes the intra-device and inter-device HDs for considering extra high-frequency components adopting a key size of m^2 (m = 30, 90, 150 and 210). One can find the trade-off between the expanded capacity and the performance (i.e., uniqueness and reproducibility). Nevertheless, the two sets of HDs are still clearly separated, which validates the PUF function. Here the estimated capacity reaches its maximum of ~ 2^{43401} (upon m = 210).

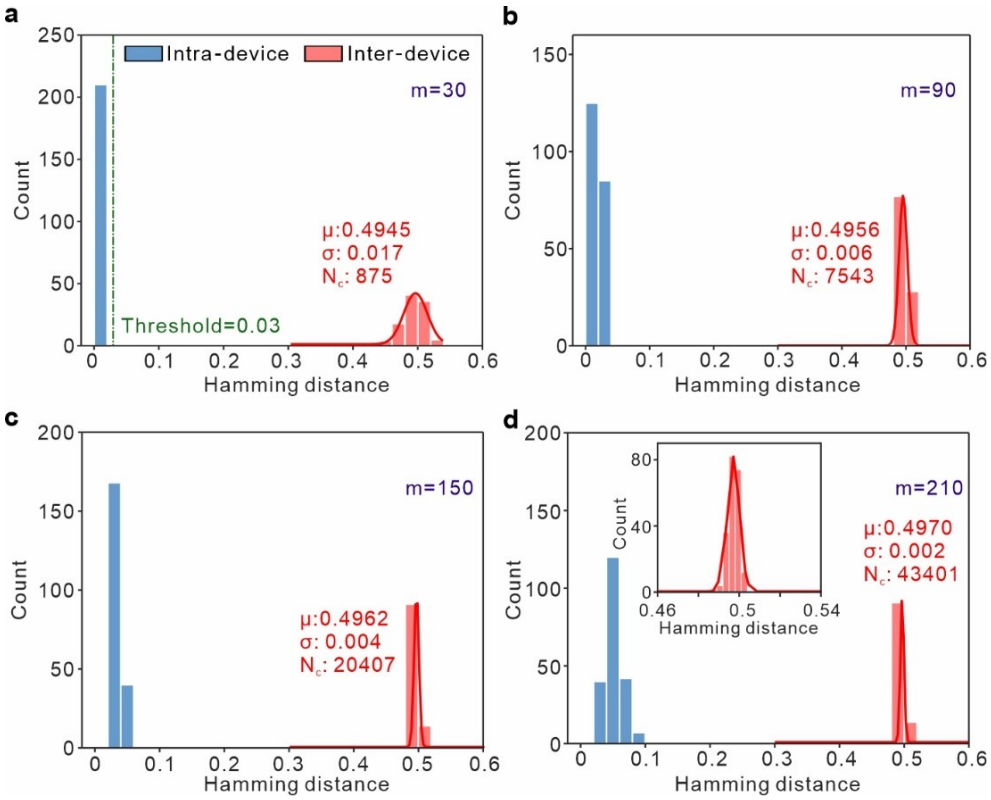

Fig. S11 Distributions of inter-device and intra-device HDs for PUF labels prepared with α = 8° when PUF key size m is 30 (a), 90 (b), 150 (c) and 210 (d). The red lines are the Gaussian fits. Inset: zoomed-in views around HD of 0.5.

Notably, upon a larger deposition angle, the probability of cluster formation is reduced and the heterogeneity might be suppressed. Therefore, the increased σ, in turn, deteriorates the uniqueness and the encoding capacity (N_c from ~ 875 at α = 8° to ~ 720 at α = 16°, see Fig. S12).

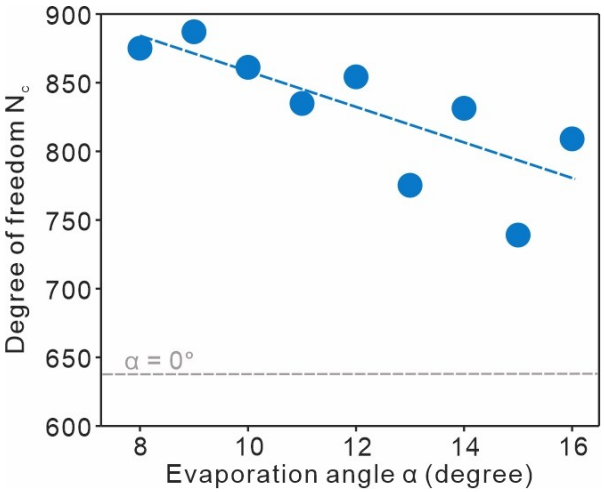

Fig. S12 Summary of estimated N_c as a function of α. The dashed line serves as a visual aid.

Section S6. Details in single challenge-different PUFs operation

In order to enhance the uniqueness of the PUF keys generated for multi-dimensional expansion, a region of 800 × 800 pixels was utilized in image processing to generate PUF keys. Figure S13(a) summarizes the 12 PUF keys generated via the multi-dimensional expanding strategy. The keys were employed as identifiers to the same challenge using a simple exclusive-OR (XOR) operation (see Fig. S13(b)).

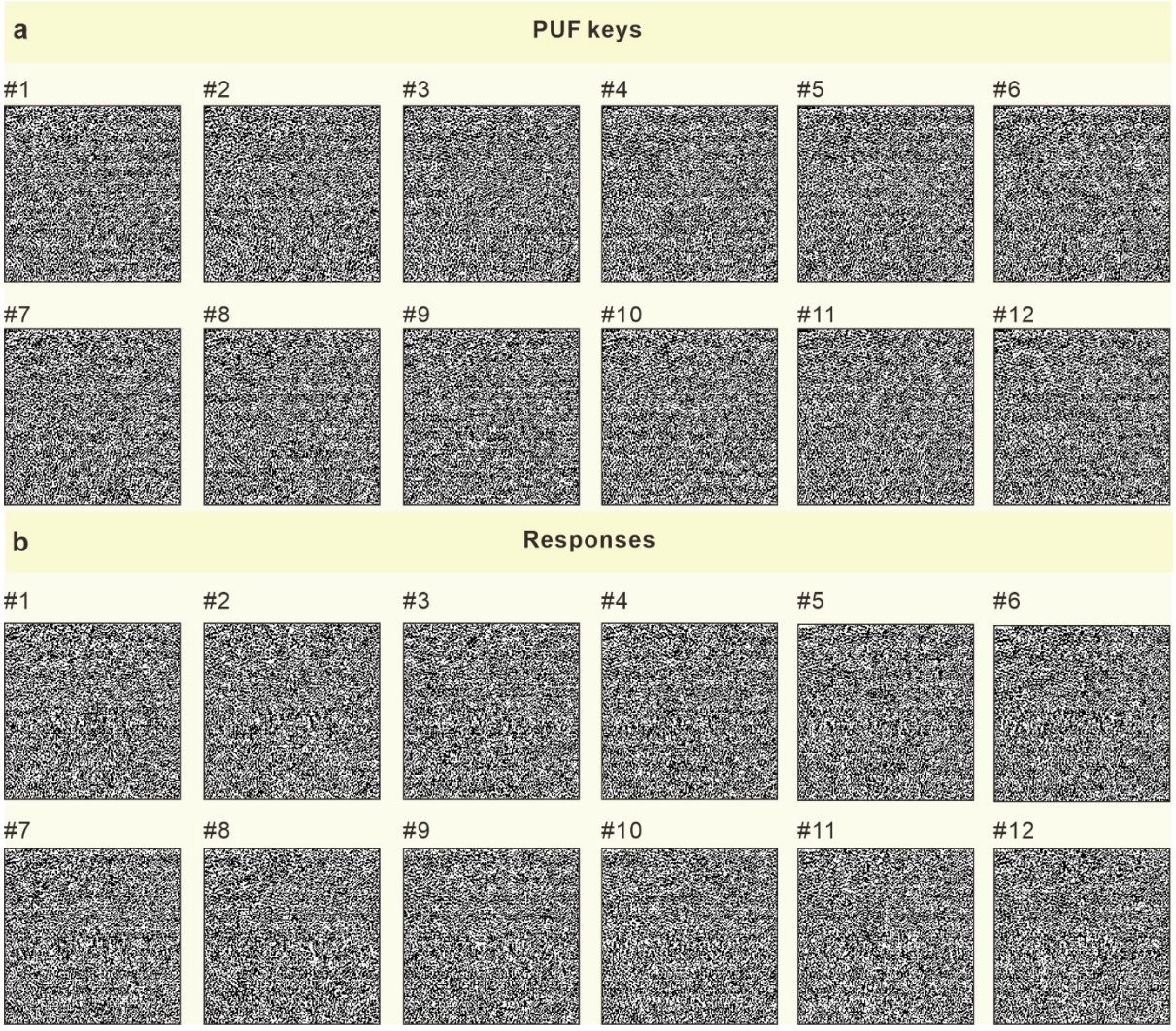

Fig. S13 (a) The 12 original PUF keys adopted for single challenge-different PUFs operation. (b) The corresponding 12 responses.

Section S7. Benchmarking of the state-of-the-art optical PUFs for anti-counterfeiting

Table S1 summarizes the recently developed optical PUFs using different optical materials and structures, which hold great potential to act as weak PUFs for anti-counterfeiting. Our work reports an integration of arrayed PUF labels on a single chip. For each PUF label, the estimated encoding capacity by calculating the number of mutually independent bits N_c reaches ~ 2^{43401}, which is the highest value among these works.

Table S1 Summary of the state-of-the-art of optical PUFs.

Year	PUF structures (materials)	Numbers of PUFs on a chip	Read mode	Encoding capability	NIST test	Expanding strategies (number of channels)	Inter- (Intra-) HD	Ref.
2016	nanoparticle (gold/silver)	1	image	-	-	-	-	13
2020	aerogels (silica)	1	image	2^{10000}	10	-	~ 0.11* (~ 0.95)	21
2021	nanofilms (copolymer)	1	image	2^{3700}	-	-	0.499 (0.038)	24
2021	crystals (phosphorescent)	21	Raman scattering	10^{2700} (DDT) 10^{7000} (Np6A)	-	-	0.18* (0.95)	22
2021	nanoparticles (diamonds & silk fibroin)	1	Raman scattering	2^{25}, 2^{2500}, 2^{10000}	-	-	~ 0.5 (~ 0.05)	30
2021	nanoparticles (gold/nickel oxide)	1	image	2^{10}-2^{10000}	-	-	~ 0.494 (~ 0.11)	14
2021	nanoislands (silver)	1	image	-	-	spectral/ morphological (3)	-	16
2022	nanoparticles (gold)	~ 100	Raman scattering	2^{25}, 2^{100}, 2^{400}	1	-	~ 0.489 (~ 0.09)	15
2022	nanoparticles (silver)	1	image	8^{7369}	-	-	-	11
2022	fibers (silk)	1	image	2^{345}	7	wavelength (3)	~ 0.499 (~ 0.03)	19
2022	nanospheres (copolymer)	1	reflection spectrum	10^{25}, 10^{400}, 10^{2500}	9	-	0.52-0.38 (0.08-0.12)	20

2022	nanofilms (organic molecule)	1	image	2^{256}	-	wavelength (3)	0.470 (~ 0.009)	38
2023	microspheres (halide perovskites)	1	PL spectrum	2^{48} (low density) 2^{52} (high density)	7	power density (2)	~ 0.5 (~ 0.05)	35
2023	nanoclusters (gold)	~ 1296	image	10^{348}	-	-	0.45* (1)	10
This Work	**nano particles &clusters (gold)**	**324**	**image**	**~ 2^{875} - 2^{43401} (single)**	**7**	**wavelength (7) & polarization (6)**	**~ 0.494 (~ 0.005)**	-

* The adopted way of evaluation is the correlation coefficient.

In addition to the estimated encoding capacity, we propose another figure of merit (FOM) to quantify the overall performance of uniqueness and reproducibility of a PUF label. Figure S14 presents the overall performance based on these two FOMs. Our proposed scalable plasmonic PUFs exhibit the superior distinguishability of $|\mu_{inter\text{-}HD} - 0.5| + |\mu_{intra\text{-}HD}|$ up to an unprecedentedly down value (~ 0.011). Meanwhile, the encoding capacity after expansion using high-frequency components reaches the highest value, while the trade-off is the moderate enhancement in the distinguishability from ~ 0.01 to ~ 0.05.

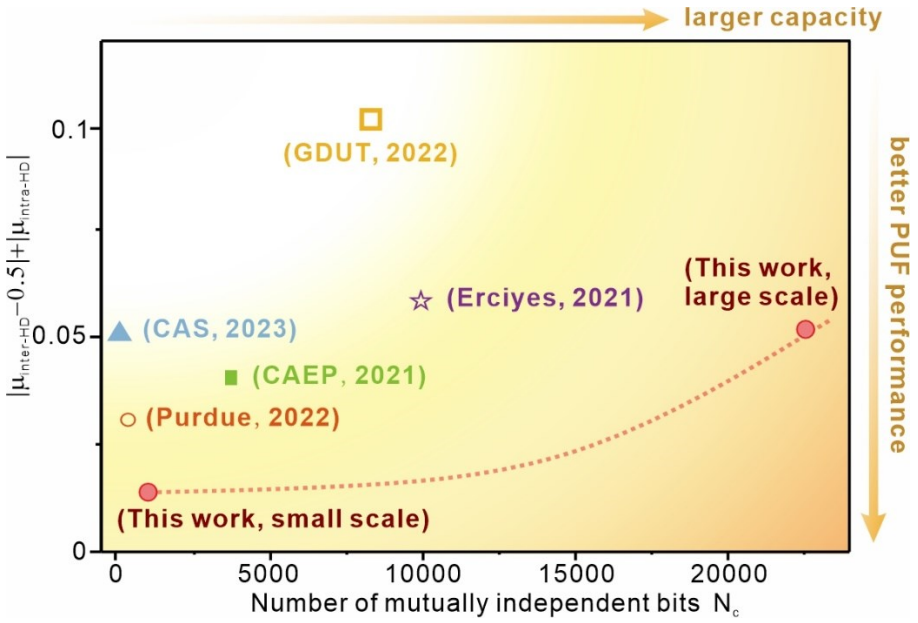

Fig. S14 The summary of two figure-of-merits, namely $|\mu_{inter\text{-}HD} - 0.5| + |\mu_{intra\text{-}HD}|$ and N_c for different optical PUF systems.

Section S8. Compact PUF system as a low-cost alternative

To better reveal the novelty of the fabrication technique, our template-assisted technique can be extended to different types of PUF materials (e.g., metals and dielectrics) and substrates (e.g., PDMS). Figure S15 presents our fabricated flexible PUF chip on a PDMS substrate (3 × 3 cm^2). The PUF integration on a flexible substrate offers elevated compatibility with different products in expanded scenarios.

Fig. S15 Picture of a fabricated flexible PUF chip on a PDMS substrate.

Furthermore, the PUF system can be operated with minimized amounts of free-space optical components, by using a low-cost, fixed-wavelength light source and a ubiquitous imager/camera (see Fig. 16(a)). In Fig. S16(b)-(c), a compact system consisting of an LED and a CMOS imager was developed. With a lensless imaging scheme, we envision that our developed plasmonic PUF chip can be operated at a cost of ~ 100-200 USD.

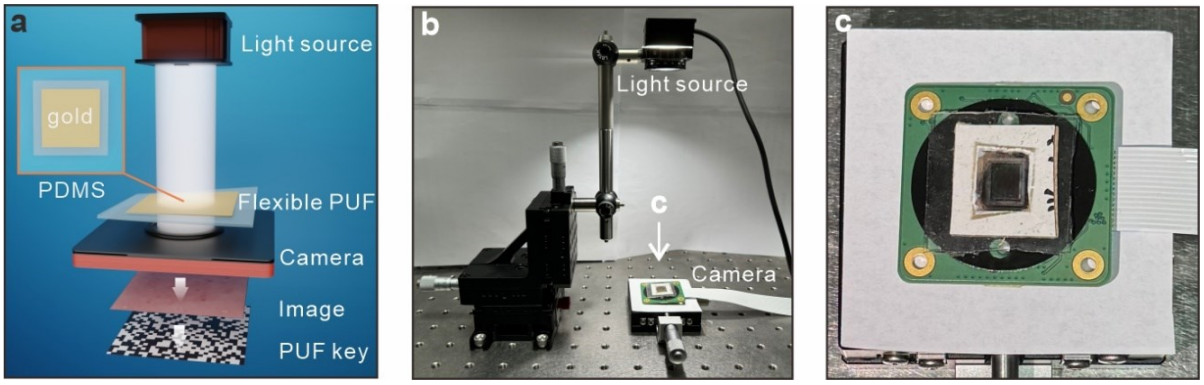

Fig. S16 (a) Schematic of a flexible plasmonic PUF chip and its readout system via lensless imaging. Inset: top view of a flexible PUF chip. (b) Picture of the readout system. (c) Picture showing the integration of a flexible chip onto a CMOS imager.

Section S9. Stability tests under mechanical stretching

We have systematically carried out tests of stability against stretching conditions using plasmonic PUFs fabricated on a PDMS-based flexible substrate (see Section S8). As shown in Fig. S17(a), upon applying a stretching length of 1.2 cm onto a PUF chip (size of 3 × 3 cm²), there is no significant visual disparity in the overall distribution of the PUF keys. Figure S17(b) summarizes the intra-device HDs under different stretching conditions (with lengths of 0.4, 0.8, and 1.2 cm respectively, each stretch length was tested five times), confirming its resilience to mechanical deformation.

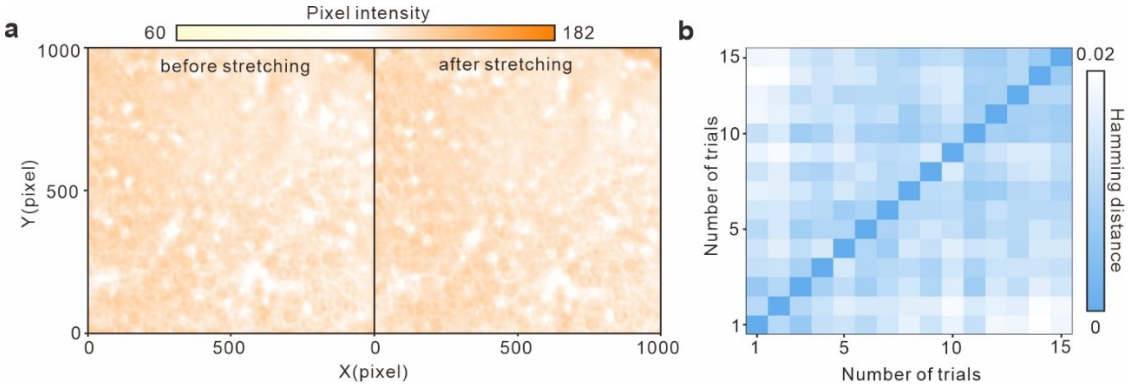

Fig. S17 (a) Captured transmission image of a single flexible PUF label before (left) and after (right) stretching. (b) Pairwise match of 15 PUF keys with different stretch lengths to examine the stability.